Inter-compartment interaction in multi-impeller mixing
Part II. Experiments, sliding mesh and large Eddy simulations

Haringa, Cees; Vandewijer, Ruben; Mudde, Robert F.

DOI
10.1016/j.cherd.2018.06.007

Publication date
2018

Document Version
Final published version

Published in
Chemical Engineering Research and Design

Citation (APA)
Haringa, C., Vandewijer, R., & Mudde, R. F. (2018). Inter-compartment interaction in multi-impeller mixing: Part II. Experiments, sliding mesh and large Eddy simulations. *Chemical Engineering Research and Design*, *136*, 886-899. https://doi.org/10.1016/j.cherd.2018.06.007

CHEMICAL ENGINEERING RESEARCH AND DESIGN 136 (2018) 886–899

Contents lists available at ScienceDirect

Chemical Engineering Research and Design

journal homepage: www.elsevier.com/locate/cherd

Inter-compartment interaction in multi-impeller mixing. Part II. Experiments, sliding mesh and large Eddy simulations

Cees Haringa[*],[1], *Ruben Vandewijer*, *Robert F. Mudde*

Transport Phenomena, Department of Chemical Engineering, Delft University of Technology, van der Maasweg 9, 2629HZ Delft, The Netherlands

ARTICLE INFO

Article history:
Received 19 November 2017
Received in revised form 24 April 2018
Accepted 1 June 2018
Available online 13 June 2018

MSC:
00-01
99-00 *Keywords:*
Mixing
Schmidt number
CFD
Multiple impellers
Rushton

ABSTRACT

Steady state multiple reference frame-RANS (MRF-RANS) simulations frequently show strong over-predictions of the mixing time in single-phase, multi-impeller mixing tanks, which is sometimes patched by ad hoc tuning of the turbulent Schmidt-number. In Part I of this work, we experimentally revealed the presence of macro-instabilities in the region between the impellers, as well as a peak in the turbulent kinetic energy in the region where the flow from the individual impellers converges. The MRF-RANS method was found unable to capture both. In this second paper, we show that the sliding-mesh RANS (SM-RANS) approach does capture the effect of macro-instabilities, while still underestimating the turbulent kinetic energy. Consequently, the SM-RANS method mildly over-estimates the mixing time, while being less sensitive to the exact mesh geometry. Large eddy simulations with the dynamic Smagorinsky model reasonably capture the kinetic energy contained in macro-instabilities, and properly assess the turbulent kinetic energy in the region between the impellers, even for crude meshes. Consequently, the mixing time is reasonably assessed, and even under-predicted at the crudest meshes. However, the turbulent kinetic energy and energy dissipation in the impeller discharge stream are poorly assessed by the dynamic Smagorinsky model.

1. Introduction

Computational fluid dynamics (CFD) has frequently been applied to simulate mixing processes in stirred tanks. Especially Reynolds averaged Navier Stokes (RANS) models provide the possibility to evaluate the mixing performance of various impeller configurations without requiring an extensive experimental campaign. An assessment of mixing literature focusing on Rushton turbines, conducted in Part I of this work, reveals that RANS simulations are capable of reasonably predicting the mixing behavior in tanks stirred by a single impeller, albeit with the requirement of high mesh densities. In contrast, the dimensionless mixing time θ_{95} is systematically over-predicted in multi-impeller tanks with high mutual impeller spacing when using RANS models. In particular, for multiple reference frame (MRF) simulations increasing mesh densities results in an increasing over-prediction of θ_{95} compared to experimental results.

It is well known that compartments form around the individual impellers of a multi-Rushton tank. In Part I of this work,

---

Abbreviations: MI, macro-instability; LDA, laser Doppler anemometry; PIV, particle image velocimetry; RANS, Reynolds averaged Navier Stokes; MRF, multiple reference frames; SM, sliding mesh; (S/R)KE, standard/realizable $k-\epsilon$; RSM, Reynolds stress model; (D/L)ES, detached/large Eddy simulation.

[*] *Corresponding author.*

E-mail address: cees.haringa@DSM.com (C. Haringa).

[1] Current address: DSM Biotechnology Center, Alexander Fleminglaan 1, 2613AX Delft, The Netherlands.

https://doi.org/10.1016/j.cherd.2018.06.007

Nomenclature

Roman

C_t	tracer concentration, kg/m^3
C	off-bottom clearance impeller, m
C_S	Smagornisky constant, –
ΔC	inter-impeller clearance, m
D	impeller diameter, m
D	diffusion coefficient, m^2/s
D_t	diffusion coefficient, turbulent, m^2/s
E_p/E_t	fraction of periodic energy in spectrum of u', –
f	frequency, s^{-1}
$f_{1.1}$	base frequency 1, s^{-1}
$f_{2.1}$	base frequency 2, s^{-1}
$f_{1.2}$	harmonic frequency 1, s^{-1}
$f_{2.2}$	harmonic frequency 2, s^{-1}
F_Q	pumping number, –
h	axial coordinate, m
H	tank height, m
k	slot number (autocorrelation), –
k_t	turbulent kinetic energy, m^2/s^2
k_{MI}	macro-instability kinetic energy, m^2/s^2
$k_{t,*}$	$k_t + k_{MI}$, m^2/s^2
$k_{t,fit}$	k_t computed via auto-correlation fit, m^2/s^2
$k_{t,SI}$	k_t computed via spectral integration, m^2/s^2
$k_{MI,fit}$	k_{MI} computed via auto-correlation fit, m^2/s^2
$k_{MI,SI}$	k_{MI} computed via spectral integration, m^2/s^2
N	impeller revolutions, 1/s
P	power, W
Po	power number, W
Q_{ax}	axial flow rate, L/s
r	radial position, m
R	tank radius, m
S_{ij}	shear rate, s^{-1}
Sc_t	turbulent Schmidt number, –
T	tank diameter, m
Δt	timestep size, s
u'	fluctuating velocity, m/s
U	mean velocity m/s
U_{tip}	impeller tip speed, m/s
V	tank volume, m^3
V_i	grid cell volume, m^3
w	Tukey–Hanning window, –

Greek

λ	laser wavelength, nm
μ	viscosity, dynamic, Pa s
μ_t	viscosity, dynamic, turbulent, Pa s
ν	viscosity, kinematic, m^2/s
ν_t	viscosity, kinematic, turbulent, m^2/s
ϵ	turbulent dissipation rate, m^2/s^3
$\hat{\rho}$	auto-correlation coefficient, –
ρ_l	density, kg/m^3
Ψ	noise component, –
τ_{lag}	lag time, s
τ_{95}	mixing time, s
τ_{ij}	stress tensor, Pa
θ_{95}	mixing number $N \cdot \tau_{95}$, –

we posed the hypothesis that the over-predicted θ_{95} originates from an under-prediction in mass exchange between these compartments, while mixing inside the compartments is likely properly captured (Coroneo et al., 2011). Although stirred tanks have been studied numerous times, the region between the impellers had previously attracted little attention. We hence focused our study on this region, to provide insight in the inter-compartment hydrodynamics and their role in mixing. Using laser-Doppler anemometry (LDA), we observed that this transport is governed by two processes: macro-instabilities (MIs) at frequencies $f/N = 0.02$–0.06 (N the agitation rate in s^{-1}) in the horizontal plane separating the compartments, and a peak in turbulent kinetic energy (k_t) in the plane segregating the compartments, generated by the collision of the flow-loops in the converging flow section near the wall. Both these effects are expected to enhance axial mass exchange.

Besides experimental results, we reported steady state MRF simulations in Part I of this study. Due to their steady state nature, they are inherently incapable of capturing the influence of macro-instabilities. Combined with an underestimated turbulent kinetic energy (k_t), attributed to poor capturing of turbulence generation in the colliding flow region by virtue of Reynolds averaging, this leads to a highly overestimated θ_{95}; θ_{95} was furthermore strongly affected by the axial flowrate between the compartments, which in turn was highly mesh sensitive. This explained the increasing θ_{95} with increasing mesh density. In this second part, we assess whether transient simulations, both sliding mesh (SM) RANS and large Eddy simulations (LES), do capture all relevant hydrodynamics between the impellers, and properly assess the mixing times in multi-impeller stirred tank systems.

2. Literature review: Rushton turbines, LES and DES

In the previous part of this work we discussed the literature regarding experimental assessment of flows in Rushton-stirred tanks, and the use of RANS models to model such flows. Mixing results for LES were also included in Part I, and are not listed here. Here, we discuss LES and detached eddy simulations (DES) for flow modeling. To our knowledge, DES has not been used for mixing studies in baffled Rushton-stirred tanks.

2.1. LES

Revstedt et al. (1998) used finite volume LES (FV-LES), with 2.12×10^5 grid cells, an implicit closure model and momentum source terms for impeller modeling. Decent results for U and k_t were reported in the bulk, with poorer agreement near the impeller. Yeoh et al. (2004, 2005) applied the Smagorinsky (SGS) subgrid model with constant $C_S = 0.1$ (FV-LES, 4.9×10^5 cells with sliding-deforming grid), reporting good results for U and k_t, but providing no data on ϵ. Zhang et al. (2006) reported similar results. A lattice-Boltzmann approach (LB-LES) is frequently applied in LES studies (Eggels, 1996). Eggels (LB-LES, SGS, $C_S = 0.1$) showed some local under-prediction of U_{ax}, but overall a good agreement with data by Bakker (1996) was reported. Derksen and Van den Akker (1999) (SGS-model, $C_S = 0.12$, 6×10^6 grid nodes) reported accurate results for the discharge stream velocities, k_t, and trailing vortex behavior. They reported a phase-averaged maximum energy dissipation in the impeller discharge of $\bar{\epsilon}_{max}/N^3D^2 \approx 4.6$, over 50% lower than measured experimentally (Ducci and Yianneskis, 2005).

Hartmann et al. (2004) reported a similar under-estimation of ϵ with LB-LES, results that are further supported by Micheletti et al. (2004) (SGS, $C_S = 0.1$) with FV-LES.

Delafosse et al. (2008, 2009) (sliding mesh, 10^6 cells, FV-LES, SGS model) explicitly noted that setting $C_S = 0.1$ leads to a significant under-prediction of ϵ in the discharge stream. $C_S = 0.1$ was selected based on testing for a wide range of flows, with higher values of C_S leading to excessive turbulence dampening. Setting $C_S = 0.2$ strongly improves predictions for ϵ, without significantly affecting the predictions for velocity and k_t. Soos et al. (2013) (sliding mesh, 1.6×10^6 cells) also used $C_S = 0.2$. Compared to the data of both Escudié et al. (2004), and Wu and Patterson (1989), they reported a mild under-prediction of the velocities and the periodic kinetic energy, while k_t was well predicted. The values for ϵ are in accordance with Delafosse et al.

The work of Delafosse et al. and Soos et al. indicates a case-by-case tuning of C_S may be required, which is undesirable from the perspective of predictive capabilities. The dynamic SGS (DYN) model aims at solving this issue by computing rather than prescribing C_S. Murthy and Joshi (2008) (FV-LES, DYN, 1.3×10^6 cells, sliding mesh) report good results for the dissipation based power number Po_ϵ, but show no profiles of ϵ or values of C_S. Jahoda et al. (2007) apply the dynamic model for mixing in 1 and 2 impeller geometries but did not report ϵ or Po_ϵ. They did show local values of C_S, which were in the range of 0.05–0.1, below the default $C_S = 0.1$.

A direct computation of C_S using direct numerical simulation (DNS) by Gillissen and Van den Akker (2012) yielded $C_S \approx 0.1$, in agreement with their own dynamic LES. This indicates that the C_S tuning conducted by Delafosse et al. and Soos et al. is not in accordance with DNS observations. Gillisen and van den Akker noted that the under-prediction in ϵ may be the result of an under-predicted k_t-production due to insufficient mesh resolution in the vicinity of walls.

2.1.1. DES

Detached eddy simulations (DES) blend a LES approach in the free-stream with RANS in under-resolved (wall) regions, and may thereby reduce any dependence of the bulk flow on wall effects, possibly improving the predictions for ϵ if the hypothesis by Gillissen is correct. Of course, the accuracy of the wall flow itself will still be limited, due to the inherent assumptions of the RANS methodology.

Gimbun et al. (2012) presented Spalart-Allmaras-DES simulations of a Rushton-stirred tank, extensively comparing the results with both *SKE-RANS* and *FV-LES* (SGS, $C_S = 0.1$). The bulk velocity prediction was very similar between the models. DES generally yields the best agreement with experimental k_t data (Derksen et al., 1999), predicting slightly higher values than *SKE* and LES. LES and DES performed similar in assessing the qualitative trailing vortex behavior, with the *SKE* model predicting significantly lower radial spreading of the vortex core, similar to the study of Singh et al. (2011). DES compared favorable to the other models in predicting velocities and k_t in the vortex core. Overall, DES outperformed RANS, and outperformed LES in regions where wall effects are significant. Chara et al. (2016) came to similar conclusions, observing good agreement in discharge velocities and trailing vortex behavior. They noted that the tangential spread of the trailing vortex is slightly narrower than experimental (PIV) results show.

Lane (2015) reported the energy dissipation behavior of various turbulence models with an A-310 impeller (13.1×10^6 grid cells). A power recovery of 69% was observed, i.e. $P_{DES} = \int(\mu + \mu_t)S_{ij}^2 dV$ is 69% of the power input based on torque. For various SST and KE formulations, the energy recovery was 68–91% and strongly mesh dependent, supporting the observations by Coroneo et al. (2011). The low energy recovery for DES, at the finest mesh used, does hint that the wall treatment of DES does not provide a significant improvement over LES in terms of resolving ϵ. A comprehensive comparison of LES and DES with various levels of wall resolution, possibly supported by DNS, is required to provide further insight in the reported under-predictions of ϵ. That is out of the current scope, however.

Table 1 – Meshes used in this work. *2IF* represents a 360° domain. The last letter(s) represent the mesh quality (C = crude, M = medium, F = fine, SF = super-fine).

Name	Cells	Domain	Methods
2IF-C	648*k*	360°	LES
2IF-M	1997*k*	360°	SM-RKE, SM-RSM, LES
2IF-F	5884*k*	360°	SM-RKE
2IF-SF	10584*k*	360°	LES

3. Materials and methods

3.1. *CFD setup*

3.1.1. *Geometry*

A 2-impeller stirred tank with $H = 2T$, $D = T/3$, $C = T/3$ and $\Delta C = T$ was modeled, with $T = 0.29$ m, and an agitation rate $N = 5\,\mathrm{s}^{-1}$. Note that our own experiments were conducted after the CFD work, and because of the equipment available in our lab were performed with $T = 0.26$ and $N = 5.78\,\mathrm{s}^{-1}$. This gives $Re = 4.34 \times 10^4$, compared to 4.67×10^4 by Jahoda et al. (2007) and in our CFD work. We do not expect the results to be affected; all results are presented in dimensionless form, and all work was conducted in the fully turbulent regime. Detailed information on the experiments is presented in Part I of this work. All internals were modeled as sheet bodies (Gunyol and Mudde, 2009; Coroneo et al., 2011). LES and *SM-RANS* Simulations were conducted with a 360° domain, as using a periodic mesh will constrain the motion of macro-instabilities (see Part I of this study). In accordance with the experimental work of Jahoda et al., the tracer concentration is tracked with two probes, the bottom probe at height T/4 and top probe at height 1.25T, placed between the baffles, at T/20 from the wall.

3.1.2. *Numerical setup*

The numerical settings were largely similar to those used in Part I. Spatial discretization was set to 2nd upwind (Gunyol and Mudde, 2009; Coroneo et al., 2011) with RANS, and bounded central differences with LES simulations. Standard wall functions were employed for all simulations. The free surface at the top was mimicked by using a no-shear surface, all walls were set to no-slip. Convergence was declared when the residuals were below 10^{-5} within a timestep. The meshes used in this work are equal to those in Part I of the work, with cell counts listed in Table 1. Due to the computation time required for *SM-RANS* and *SM-LES*, it was not possible to test all models with all meshes. Additional information on the meshes is provided in Supplementary material A.

Tracer was injected in a spherical volume with a radius of 0.0125 m; the volume center was at $y = 0.551$ m (from the bottom), at $r = 0.0725$ m, in the baffle plane. We set $\Delta t = 0.00333$ s with sliding mesh and the *2IF-C* LES simulation. The *2IF-SF*

LES simulation was conducted with $\Delta t = 0.001667$ s. Mixing in mesh *2IF-M* was studied in triplicate with LES; twice with $\Delta t = 0.00333$ s, and once with $\Delta t = 0.001667$ s, to test how reproducible the results are. Temporal discretization was second order implicit. The tracer and bulk fluid had equal properties, $\rho = 1000$ and $\mu = 0.001$, such that the tracer will not disturb the flowfield. Subgrid species diffusion is coupled to the subgrid turbulent viscosity μ_t via the turbulent Schmidt number, $Sc_t = \mu_t/(\rho D_t) = 0.7$, giving a species flux $J_i = -(\rho_l D + \mu_t/Sc_t)\nabla C_i$ with $D = 10^{-9}$ the molecular diffusion coefficient and C_i the scalar concentration.

3.2. *Turbulence models*

The realizable $k - \epsilon$ (RKE) and Reynolds stress model (RSM) used in SM-RANS modeling are well established, we refer to, e.g. Gunyol and Mudde (2009) for their description. Based on previous literature, we focus on the dynamic Smagorinsky (LES-DYN) model for LES. This model assumes isotropic subgrid turbulence, using an eddy viscosity formulation with μ_t being the subgrid turbulent viscosity. The filtered Navier–Stokes equations for an incompressible fluid read:

$$\frac{\partial \bar{u}_i}{\partial t} + \bar{u}_i \frac{\partial \bar{u}_i}{\partial x_j} = -\frac{1}{\rho}\frac{\partial \bar{p}}{\partial x_i} + \frac{\partial}{\partial x_j}\left([\nu + \nu_t] \frac{\partial \bar{u}_i}{\partial x_j} \right) \tag{1}$$

Here, ν_t is the kinematic turbulent viscosity, μ_t/ρ. The dynamic turbulent viscosity μ_t is calculated from Eq. (2)

$$\tau_{ij} - \frac{1}{3}\tau_{kk}\delta_{ij} = -2\mu_t \bar{S}_{ij} \tag{2}$$

With S_{ij} is the resolved-scale rate of strain tensor. The subgrid-scale stress tensor τ_{ij} is calculated by the applied subgrid model. The basis of the dynamic subgrid model (LES-DYN) is formed by the turbulent viscosity formulation of the standard Smagorinsky model, Eq. (3):

$$\mu_t = \rho L_s^2 \cdot \sqrt{2\bar{S}_{ij}\bar{S}_{ij}} \tag{3}$$

where L_s is the mixing length calculated as $L_s = \min(\kappa d, C_S V_c^{1/3})$ with κ the Von Karman constant, d the nearest wall distance and C_S the Smagorinsky constant. Whereas the standard Smagorinsky model typically prescribes $C_S = 0.1$, the dynamic model computes C_S based on the local resolved motions using a test-filter approach based on the work of Germano et al. (1990) and Lilly (1992). We refer to Kim et al. (2004) for details on the implementation in FLUENT. For stability, C_S is capped between 0 and 0.23.

3.3. *Analysis methods*

We recorded velocity time series in the baffle plane in our LES simulations. In the impeller outflow, the impeller frequency and the first and second harmonic thereof were removed via Eq. (6), similar to the experimental procedure reported in Part I. Data in the region between the impellers, referred to as the inter-compartment region (with the horizontal plane segregating the compartments referred to as inter-compartment plane), was analyzed for the presence of MIs. The velocity time series at the points coinciding with the experimentally used grid were analyzed by fitting the auto-correlation signal (Eq. (4)) and by analysis of the spectral density function (Eq. (5)), equal to the experimental assessment:

$$\hat{\rho}_{fit}(\tau) = b + c_0 e^{-\alpha_0 \tau} + \Sigma_{n=1}^{i} c_n e^{-\alpha_n \tau} \cos(2 \cdot nf\pi\tau) \tag{4}$$

$$S(f) = \frac{\Delta t}{\pi}\left[\frac{1}{2}\hat{\rho}(k\Delta\tau_{lag}) w(k\Delta\tau_{lag}) \cos(kf\Delta\tau_{lag})\right] \tag{5}$$

For these methods, the influence of periodic components can be removed from the fluctuating velocity via Eq. (6) in case of the auto-correlation signal, and Eq. (7) in case of the spectral density function:

$$u'_t = u' \cdot \sqrt{1 - \Sigma(c_n)} \tag{6}$$

$$u'_t = u' \cdot \sqrt{1 - \frac{E_p}{E_t}} \tag{7}$$

Here E_p/E_t is the fraction of energy contained in the macro-instability components of the u'-spectrum; we assumed all frequencies below $f/N = 0.1$ contribute to E_p. The influence of macro-instabilities in the inter-compartment region was addressed with both methods for LES simulations. In this case, two base frequencies and their first harmonics were included in Eq. (6). In the inter-compartment region, k_t is the turbulent kinetic energy based on u'_t, k_{t^*} the total fluctuating energy, and the macro-instability kinetic energy $k_{MI} = k_{t^*} - k_t$. Subscripts *fit* and *SI* are used to distinguish between results calculated using Eqs. (6) and (7), respectively. For sliding mesh simulations, there is no turbulent component in the fluctuating velocity, hence k_{MI} was directly computed from the fluctuating Reynolds-averaged velocity, while k_t is provided by the turbulence model, and k_{t^*} follows from their sum. The location $y = 0$ is used to indicate the horizontal plane exactly between the two impellers, at a height 5T/6. A detailed discussion of the experimental analysis methods is provided in Part I of this paper.

4. Results and discussion

4.1. *Validation: the impeller outflow*

In Fig. 1, the impeller discharge stream profiles are shown, in comparison to experimental results from literature as well as Part I of this work. Experimental data on ϵ was not collected in the current study due to limitations in the equipment. As for the MRF simulations in Part I, the SM simulations show good agreement with experimental data in the impeller outflow. Again, the *RSM* simulation predicts a decrease in k_t and ϵ near the blade tip, where the *RKE* model does not. In the bulk of the outflow, *RKE* and *RSM* are in excellent agreement. LES is well capable of capturing U_{rad}, but performs poorer for k_t and especially for ϵ. Power numbers and additional discussion on mesh dependency are available in Supplementary material A.

For the LES simulations, k_t is computed based on the resolved scales, removing periodic components (blade passages) by Eq. (6). Subgrid kinetic energy is not included in the figures, which means *2IF-SF* is expected to yield higher k_t than *2IF-C* and *2IF-M*, as is indeed observed. However, *2IF-SF*, which is still insufficiently fine to capture all energy carrying eddies, does over-estimate the experimental k_t. The dissipation rate ϵ on the other hand is strongly underestimated. Overall, the power number on energy dissipation fluctuates around $Po_\epsilon \approx 8$, whereas the experimental value is $Po \approx 11$. Hartmann et al.

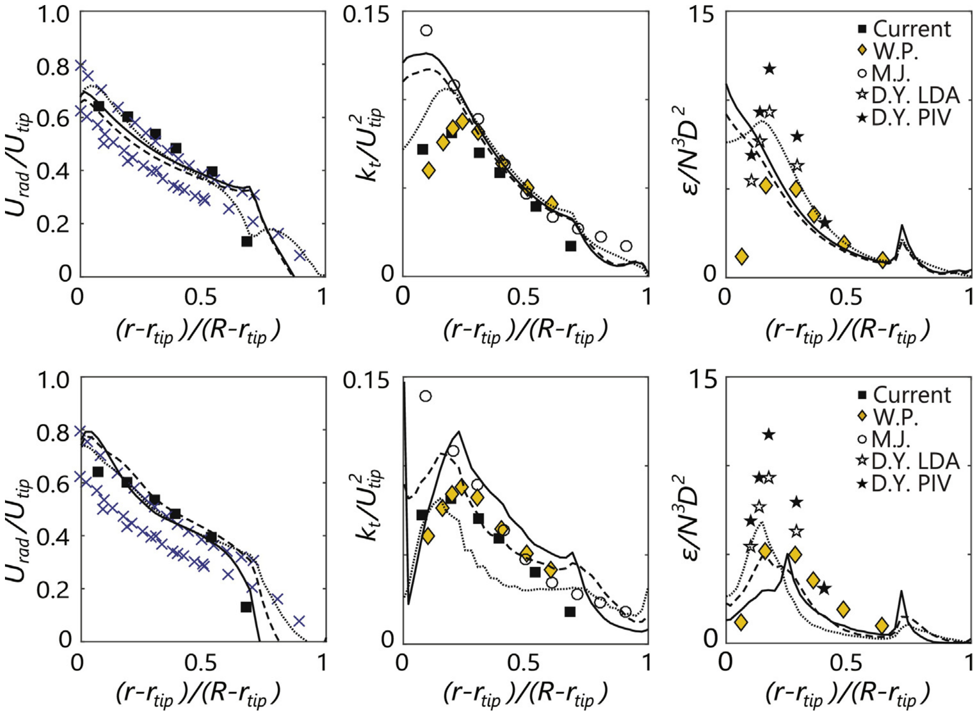

Fig. 1 – Profiles of U_{rad}, k_t and ϵ in the top impeller outflow compared with LDA data. Bottom impeller results are omitted due to similarity. Top row: SM simulations. Solid line: *2IF-F*, *SM-RKE*. Dashed line: *2IF-M*, *SM-RKE*. Dotted line: *2IF-M*, *SM-RSM*. Bottom row: LES simulations. Solid line: *2IF-SF*. Dashed line: *2IF-M*. Dotted line: *2IF-C*. Symbols represent experimental data. Abbreviations: W.P. = Wu and Patterson (1989), M.J. = Murthy and Joshi (2008), D.Y. = Ducci and Yianneskis (2005). The blue crosses in the U_{rad} plot represent the upper- and lower bound of the studies reviewed by Ranade and Joshi (1990).

(2004) and Derksen and Van den Akker (1999) reported an under-estimation of ϵ with the standard Smagorninsky model using constant $C_S = 0.1$. Delafosse et al. and Soos et al. found that setting $C_S = 0.2$ increased agreement; ϵ is highly sensitive to C_S. In agreement with Jahoda et al. (2007), we observe the dynamic model yields C_S in the range 0.01–0.06. These low C_S values are consistent with the strong under-prediction of ϵ (Delafosse et al., 2008). Unfortunately, Jahoda et al. do not report k_t and ϵ for verification. Clearly, accurate prediction of ϵ in stirred tanks using LES requires further attention.

4.2. *Mixing times*

The mixing time is reported in dimensionless form, $\theta_{95} = N\tau_{95}$, with τ_{95} being the time in seconds beyond which $C_t/\bar{C}_t$ is bound between 0.95 and 1.05, with C_t the tracer concentration. The CoM quantifies mixing in the entire domain, and is defined as Eq. (8):

$$\text{CoM} = \sqrt{\left(\frac{\Sigma_i\left((C_{t,i} - \bar{C}_t)/\bar{C}_t\right)^2 \Delta V_i}{\Sigma_i \Delta V_i}\right)} \tag{8}$$

where $\theta_{95,\text{CoM}}$ is achieved when CoM < 0.0283 (Hartmann et al., 2006). The results for all *SM-RANS* and LES simulations are given in Table 2. SM simulations predict a probe-based $\theta_{95} \approx 110$ for *RKE* based on the bottom probe, in agreement with the SM simulation of Jahoda et al. (2007), and 15% above the experimental value, both for the bottom and top probe. Overall, θ_{95} predicted with *SM-RKE* is consistently lower than with *MRF-RKE* (Part I) at the same mesh, which implies that either turbulent mass exchange between the compartments (μ_t) is higher in SM simulations, or MIs, which are inherently suppressed in *MRF* simulations, result in a higher inter-compartment mass exchange. Probe profiles, reported in Fig. 2A for *MRF* and SM, hint at the latter: whereas the *MRF* results show a constant increase in dimensionless concentration $C_t/\bar{C}_t$, wiggles in the profiles for SM hint at the presence of oscillatory motions in the inter-compartment plane.

Table 2 – Comparison of dimensionless mixing times θ_{95} for the SM-RANS and SM-LES methods, for the meshes studied in this work. *bot* and *top* represent the probe-based results, *CoM* the coefficient of mixing. The work of Hartmann is followed to set the CoM-boundary.

Mesh	**bot**/top	CoM
2IF-M-SMRKE	**112.7**/89.5	126.5
2IF-F-SMRKE	**110.1**/84.9	122.0
2IF-M-SMRSM	**133.3**/107.9	147.0
2IF-C-LES	**80.0**/71.1	86.0
2IF-M-LES ($\Delta t = 1.67$ ms)	**80.7**/69.6	88.0
2IF-M-LES ($\Delta t = 3.33$ ms, run 1)	**81.6**/69.6	n.m.
2IF-M-LES,($\Delta t = 3.33$ ms, run 2)	**78.5**/71.4	n.m.
2IF-SF-LES	**94.0**/79.1	99.0
Jahoda (LES)	**81.5**/n.r.	n.m.
Jahoda (EXP)	**92.0**/≈75	n.m.

n.m. = not measured, n.r. = not reported.

The *SM-RKE* results are similar for both meshes, for probe dynamics as well as θ_{95}. Reasonable similarity is observed in inter-compartment hydrodynamics between the meshes (see Section 4.3), in contrast to MRF-RKE in Part I. This gives some confidence that the near-equal θ_{95} is a sign of mesh independence for *SM-RKE*. The results from Part I, however, show that data for *SM-RKE* on mesh *2IF-SF* is required in order to make such a statement with confidence; the computational requirements did not allow us to conduct such a simulation within this project. More generally, the *MRF* results were highly sen-

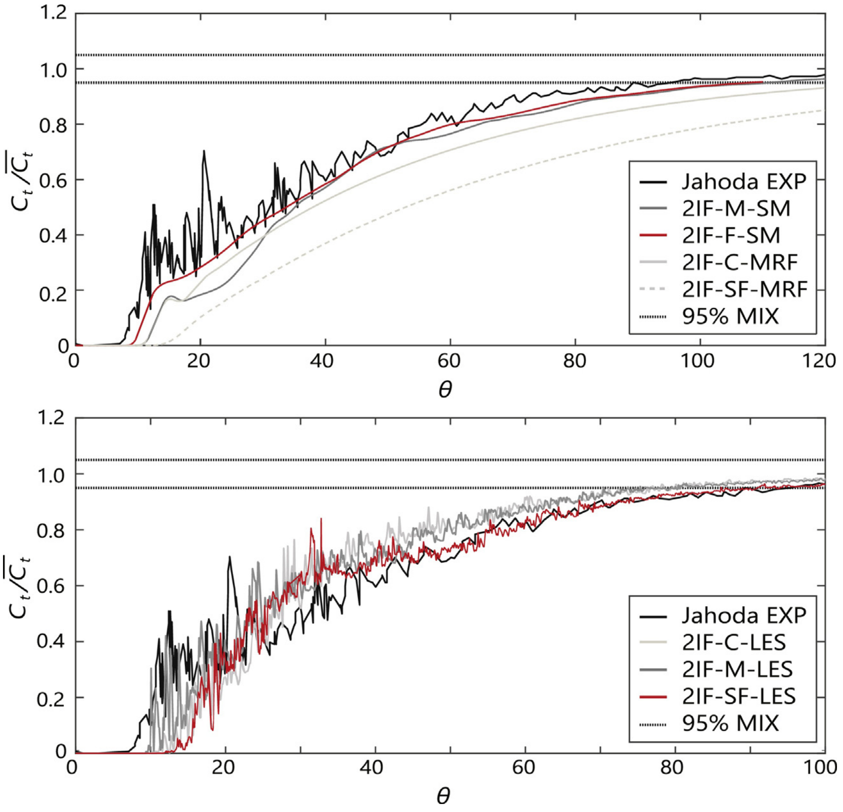

Fig. 2 – Mixing profiles for different simulations (bottom probe signal). Black: typical experimental data, Jahoda et al. (2007). Top: RANS simulations, including 2 MRF simulations (reported in Paper I). Bottom: LES simulations.

sitive to differences in Q_{ax} between the meshes, due to the flowfield being frozen during mixing. For sliding mesh simulations, the dynamic rather than frozen inter-compartment flowfield is expected to lead to a lower mesh sensitivity than was observed with *MRF*. Only one *SM-RSM* simulation was conducted, yielding a higher θ_{95}, as well as shifted inter-compartment plane (see Section 4.3). In general, the inclusion of turbulence anisotropy does not seem to improve the agreement with experimental data, in the SM simulations, MRF simulations of Part I, and single-impeller work of Gunyol and Mudde (2009). Hence, there appears to be little reason to opt for the more computationally expensive RSM model Rushton-stirred tank applications, and we did not explore *SM-RSM* at finer meshes.

The LES simulations with 2*IF-C* and 2*IF-M* yield $\theta_{95} \approx 80$ based on the bottom probe, in agreement with $\theta_{95} = 81.5$ observed by Jahoda et al., using a similar mesh density. No effect of the timestep size is observed for 2*IF-M*. Simulation 2*IF-SF* yields $\theta_{95} = 94$, in very good agreement with the experimental value $\theta_{95} = 92$ reported by Jahoda et al. (2007). The bottom-probe response profiles for LES are shown in Fig. 2B. It must be kept in mind that the figures show single realizations, except for LES runs with mesh 2*IF-M*. The results for this case show limited variation in θ_{95}, which gives confidence the difference in θ_{95} between this mesh and 2*IF-SF* is not due to regular variability in the LES method. For the top probes, θ_{95} is in line with the rough estimation made from the mixing profiles of Jahoda et al. Additional probe results, studying the sensitivity of the response to probe location, are reported in Supplementary material B.

4.3. *Inter-compartment dynamics: sliding mesh*

SM simulations predict a lower θ_{95} than MRF, although they still over-estimate the experimental value. The wiggles in Fig. 2 hint the difference between MRF and SM lies in the inclusion of MIs. Inter-compartment data (Fig. 3) shows k_{t^*} is higher for SM simulations than for MRF due to the inclusion of k_{MI}, which is 0 in MRF simulations by construction. Compared to the experiments, k_{t^*} is still under-estimated everywhere except nearest to the shaft; hence θ_{95} in SM simulations still exceeds the experimental observation. For $SM-RKE$, k_{t^*} is quite similar between the two meshes, but the contribution by k_{MI} differs: approx. 10–25% for mesh 2*IF-F*, and 5–60% for 2*IF-M*. Close to the wall, k_{MI} is in decent agreement with experimental data for 2*IF-M*, but due to an under-estimation of k_t, $k_t{}^*$ is lower overall.

U_{rad} is well captured by *SM-RKE*, although the MRF simulations performed slightly better in quantitatively capturing U_{ax}; still, the reversal from converging to diverging flow is reasonably captured with *SM-RKE*. *SM-RSM* performs poorly: a shift in inter-compartment plane position is clearly observed in the profiles for U_{rad}, U_{ax} and k_{t^*}. In contrast to the MRF simulations, reported in Part I, this does not reduce θ_{95} for SM-RSM. In the MRF simulations, a shift in the inter-compartment plane position was associated with a higher axial flowrate Q_{ax} between the compartments. The frozen plane position meant this higher Q_{ax} led to consistently faster mixing. In contrast, in SM simulations the inter-compartment plane position is dynamic, which implies that even if the plane position is shifted somewhat, this does not result in a consistent increase of mass exchange between the compartments.

Probing U_{ax} at several points in the inter-compartment region (*SM-RKE*) reveals strong oscillations in the Reynolds-averaged velocity, as shown in Fig. 4A and B. Since there are no turbulent oscillations in the Reynolds-averaged velocity profile by construction, there is no need for auto-correlation fitting to determine k_{MI}. Therefore, the MI frequencies were estimated using the more straightforward approach of taking

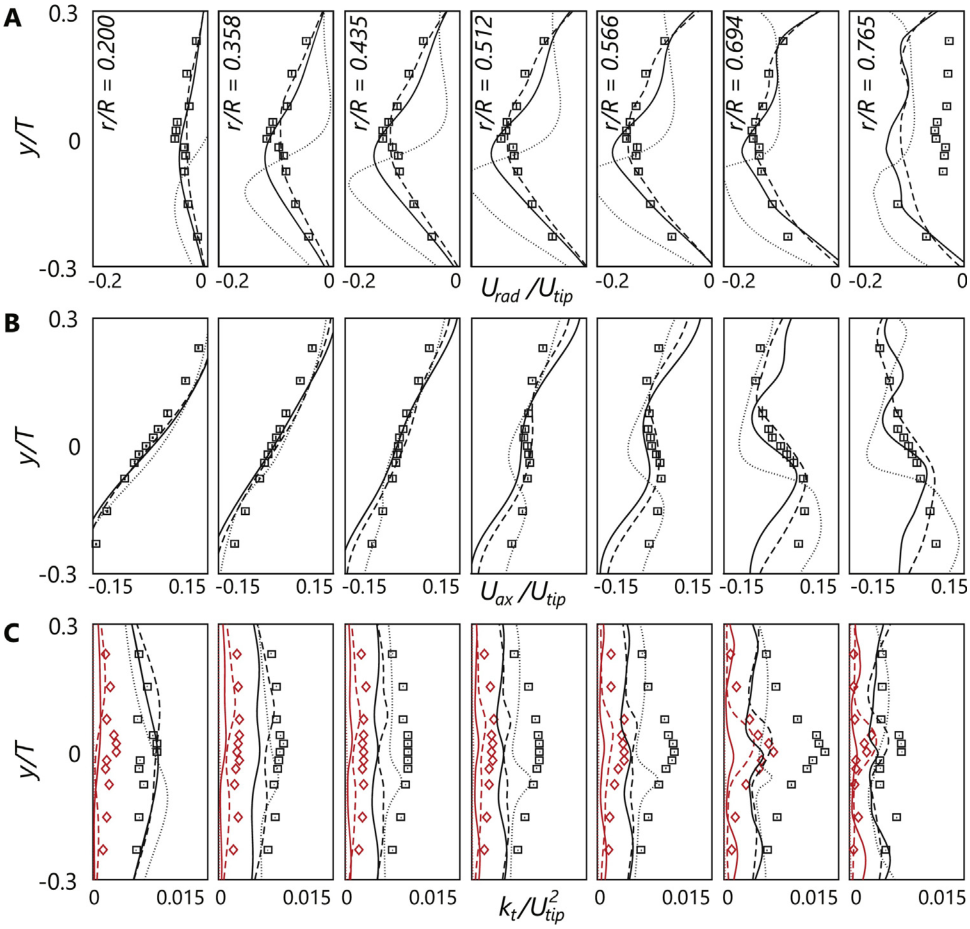

Fig. 3 – Axial profiles (baffle plane) of (A): U_{rad}, (B): U_{ax}, (C): k_t, comparing LDA results (symbols) with SM-CFD data (lines). In (C(, the black rectangles represent the total kinetic energy k_{t^*}, the blue diamonds the turbulent kinetic energy k_t, and the red diamonds the MI energy k_{MI}. The black lines represent k_{t^*}, the red lines k_{MI}. Lines: CFD results at different mesh densities (dotted: 2*IF-M*, *RSM*, dashed: 2*IF-M*, *RKE*, solid: 2*IF-F*, *RKE*). (For interpretation of the references to color in this figure legend, the reader is referred to the web version of this article.)

the Fourier spectrum. The spectrum shows velocity oscillations are highly periodic for 2*IF-M* (Fig. 4C), with a dominant frequency $f/N = 0.058$ and its harmonics. This is in excellent agreement with the jet instability frequency reported by Paglianti et al. (2008), and the value observed experimentally in Part I of this work. Experimentally, we also observed a weak contribution of $f/N = 0.02$, and strong contribution of $f/N \approx 0.04$ in the parallel flow region. A very weak $f/N = 0.02$ can be observed with SM, while $f/N = 0.04$ is absent. Case 2IF-F shows more scatter (Fig. 4D); the dominant peak now is at $f/N = 0.045$ with a strong shoulder at $f/N = 0.06$ for $r/R = 0.512$ and $r/R = 0.694$. This is qualitatively more in line with experimental observations, although the contribution of $f/N = 0.06$ is too low. At $r/R = 0.694$, an additional peak is observed at $f/N \approx 0.01$, which represents the very slow oscillation visible in Fig. 4B that is absent in Fig. 4A.

The qualitative experimental observation that axial oscillations increase with increasing radial position is captured by SM simulations. The next question is how much MIs contribute to mixing. Fig. 5 shows the velocity vectors in an axial cross section (baffle-plane) at several moments though a macro-oscillation. During the oscillatory motion, cross-over flow from the top to bottom compartment connects the downward near-wall flow in the top compartment, to flow along the shaft towards the impeller in the bottom compartment (Fig. 5B and D). Tracer concentration snapshots (Fig. 6) confirm that tracer transport between the compartments occurs dominantly along the shaft. Near the wall, the parallel-flow plane segregating the compartments is displaced as a whole with no visible inter-compartment transport. Videos of inter-compartment mixing are available online, for an *MRF-RKE*, SM-*RKE* and LES simulation.

4.4. *Inter-compartment dynamics: large Eddy simulations*

The velocity components resolved in LES span a much wider range of frequencies, well into the turbulent domain. Hence, we analyze them with the same methods as the LDA data in Part I: fitting of the velocity signal auto-correlation with dampened cosines (Eq. (4)), and spectral integration (Eq. (5)). For spectral integration, the cut-off frequency between MIs and regular turbulence was set at $f/N = 0.1$; the energy contained in the spectral range $f/N < 0.1$ is fully attributed to k_{MI}. This may be an over-estimation of the true MI energy, but because the same cut-off was used in LDA, this method provides the most direct comparison. Due to the negligible difference between simulations with $\Delta t = 0.0033$ and $\Delta t = 0.001667$, the reported results for 2*IF-M* are obtained with $\Delta t = 0.0033$, for which more date was available.

Similar to the experimental procedure, the auto-correlation signal was fitted with 2 frequency components ($f_{1.1}$ and $f_{2.1}$) and their first harmonics ($f_{1.2}$ and $f_{2.2}$). Fig. 7 shows the fits for simulations 2*IF-M* and 2*IF-SF*, at 3 radial

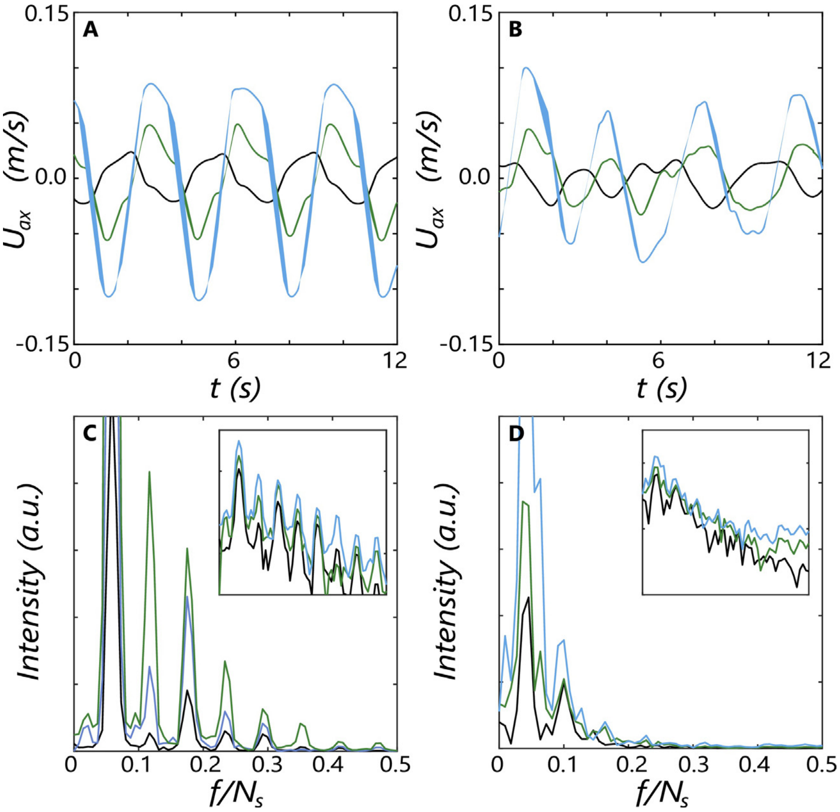

Fig. 4 – (A) Axial velocity at y = 0 versus time, *2IF-M SM-RKE*. (B) Axial velocity at y = 0 versus time, *2IF-F SM-RKE*. (C) Fourier transform of A; inset shows the same graph on a log scale. (D) Fourier transform of B; inset shows the same graph on a log scale. Black line: *r/R* = 0.2. Blue line: *r/R* = 0.512. Light blue line: *r/R* = 0.694. (For interpretation of the references to color in this figure legend, the reader is referred to the web version of this article.)

Table 3 – Axial RMS-velocity, oscillation frequencies and their contributions for *2IF-M-LES* and *2IF-SF-LES* in the plane y = 0 at different radial positions, using the periodic-fitting approach. The coefficient *c* represent the contribution to the Reynolds stress $u'u'$, with $c_{i,j}$ the *j*th harmonic of frequency component *i*. For brevity, only u'_{ax} is reported, tables for u'_{rad} and u'_{tan} are in *supplementary material C*. Top rows: 2IF-M. Bottom rows: 2IF-SF.

r/R	0.200	0.358	0.435	0.512	0.566	0.694	0.765
$u'_{ax,M}$ (m/s)	0.089	0.111	0.126	0.147	0.164	0.181	0.148
$c_{1.1,ax,M}$	0	0.026	0	0.001	0.022	0	0
$c_{1.2,ax,M}$	0.033	0.011	0.033	0.08	0.117	0.110	0.049
$c_{2.1,ax,M}$	0.002	0.005	0	0.007	0	0.015	0.023
$c_{2.2,ax,M}$	0.003	0.071	0.017	0.141	0.065	0.045	0.039
$f_{1.1,ax,M}/N$	0.014	0.010	0.012	0.012	0.012	0.012	0.013
$f_{2.1,ax,M}/N$	0.019	0.022	0.017	0.021	0.018	0.022	0.023
$10^3 \cdot k_{t,fit,M}/U_{tip}^2$	9.35	8.98	9.59	9.36	9.84	9.91	7.00
$10^3 \cdot k_{MI,fit,M}/U_{tip}^2$	1.21	2.32	1.42	1.92	1.89	1.41	0.63
$u'_{ax,SF}$ (m/s)	0.088	0.106	0.117	0.132	0.148	0.208	0.174
$c_{1.1,ax,SF}$	0	0	0.042	0.068	0.086	0.135	0.088
$c_{1.2,ax,SF}$	0.011	0.007	0	0.014	0	0	0.039
$c_{2.1,ax,SF}$	0	0	0.005	0	0	0.013	0
$c_{2.2,ax,SF}$	0.022	0.09	0.006	0.030	0.006	0.210	0.108
$f_{1.1,ax,SF}/N$	0.034	0.026	0.010	0.024	0.020	0.022	0.023
$f_{2.1,ax,SF}/N$	0.043	0.042	0.042	0.036	0.040	0.036	0.035
$10^3 \cdot k_{t,fit,SF}/U_{tip}^2$	6.48	8.22	8.90	7.37	8.28	10.2	8.06
$10^3 \cdot k_{MI,fit,SF}/U_{tip}^2$	1.80	1.01	0.60	1.89	1.62	4.00	2.10

positions at axial position y = 0. The dominant frequencies for axial oscillations in LES simulations are less sharp than the experimental frequencies reported in Part I, leading to a poorer fit quality. On average, *2IF-SF* gives $f_{1.1}/N \approx 0.023$ and $f_{2.1}/N \approx 0.039$, albeit with significant variation between radial locations. For f_2, the harmonic $f_{2.2}/N \approx 0.078$ has a higher magnitude that $f_{2.1}/N$. These frequencies lie around the experimental value of $f_{2.1}/N \approx 0.06$, which itself is not observed in *2IF-SF*. The LES data furthermore hints at the presence of higher frequency oscillations, which are not captured in the current auto-correlation fit. For the axial oscillations at mesh *2IF-M*, $f_{1.2}/N \approx 0.024$ has a relatively high magnitude, and is nearly equal in frequency to $f_{2.1}$. Harmonic $f_{2.2}/N \approx 0.04$ also has a high magnitude. While this frequency was relatively prominent experimentally, the strongest experimental component $f/N \approx 0.06$ is again not observed

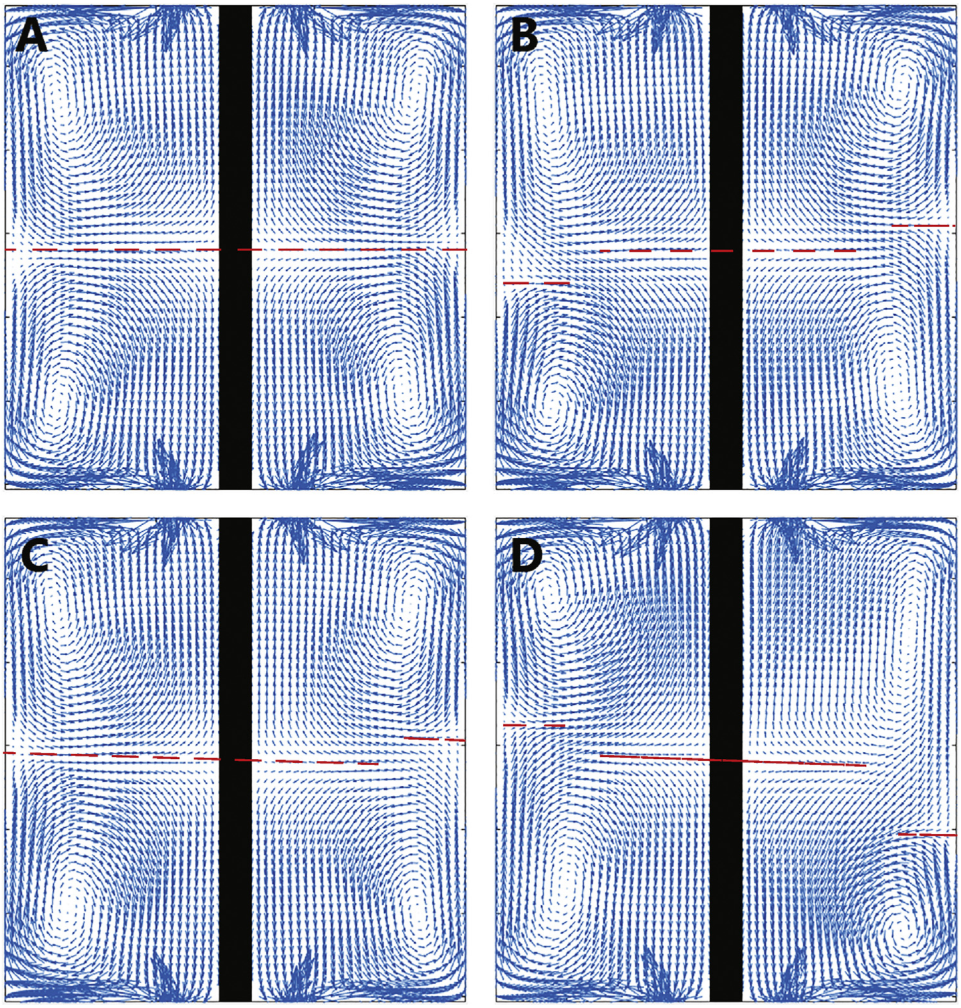

Fig. 5 – Velocity vector fields (*2IM-RKE*) during four stages of a macro-oscillation. The dashed red lines indicate the regions where $U_{ax} \approx 0$, showing that throughout the oscillations the axial separation between the compartments is locally broken, resulting in enhanced inter-compartment mixing.

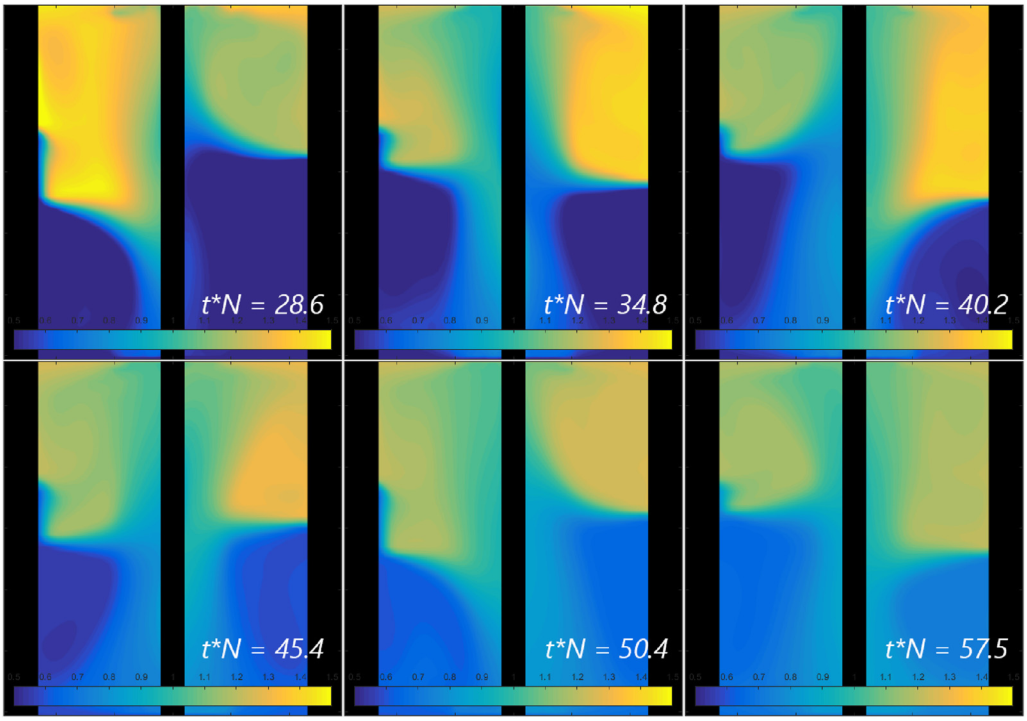

Fig. 6 – Snapshots of mixing at 6 timepoints, *2IF-M-SM*, showing tracer exchange along the shaft is influenced by MIs (video available online).

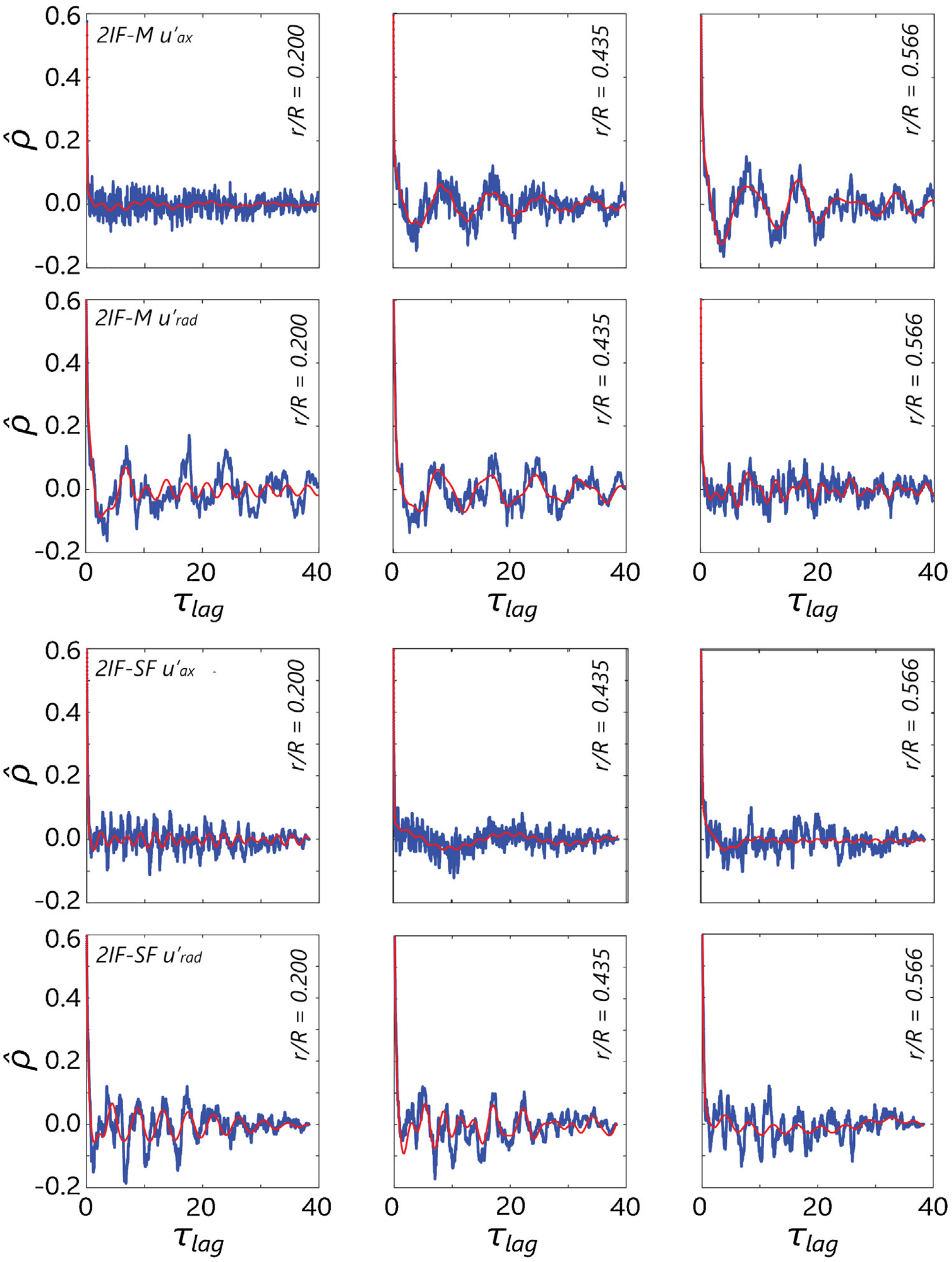

Fig. 7 – Fitted auto-correlation functions for 2*IF-M-LES* (top) and 2*IF-SF-LES* (bottom) at y = 0, at 3 radial positions. Blue line: raw data. Red line: fitted damped cosine function (see Part I for details). (For interpretation of the references to color in this figure legend, the reader is referred to the web version of this article.)

in the simulation. As with the SM simulations, the radial oscillations have a high magnitude near the shaft, dampening with increasing radial position, while the opposite is observed for axial oscillations (Table 3).

The spectral density functions (Fig. 8) show an f^{-1} scaling for $0.1 < f/N < 1$, and an $f^{-5/3}$ scaling for $f/N > 1$, in line with experimental observations. The moderate spatial resolution of the meshes results in a quick deviation from $-5/3$ scaling at the high-frequency end of the spectra. For the 2*IF-SF* simulations, the filter length ratio was around $\Delta/\eta = 10-25$ with η the Kolmogorov length scale, the lower value near the shaft and the higher near the baffle. A finer mesh may be desired, but for routine use without super-computing facilities, 2*IF-SF* is already much too demanding.

In the low frequency range, the spectral density functions confirm the observations made in the auto-correlation fits. The spectrum for 2*IF-M* does show the bi-modal peak observed experimentally, but at the lower frequencies $f_{1.2}/N \approx 0.024$ and $f_{2.2}/N \approx 0.04$, whereas experimentally $f/N = 0.045$ and 0.06 were observed. In 2*IF-SF* the bimodal peak is not observed. Here $f_{1.1}/N \approx 0.026$ and $f_{2.2}/N \approx 0.078$ contribute most, but, as in the auto-correlation data, $f/N \approx 0.045$ is absent.

Both the auto-correlation fit and spectral density method provide an estimate of the percentage of fluctuating kinetic energy that is contained in MIs. First we report results for the auto-correlation method. Using this method, $k_{MI,fit}$ 10–20% of k_{t^*} at the measured locations in the plane y = 0 for 2*IF-M*, with the maximum at $r/R = 0.358$. 2*IF-SF* yiels $k_{MI,fit}$ is 5–30% of k_{t^*}, with the maximum at $r/R = 0.694$. For comparison, experimental data yielded a contribution of 8–20% with the maximum at $r/R = 0.694$ when using the auto-correlation method. Spectral integration gave an MI contribution is $k_{MI,SI}$ is 25–30% of k_{t^*} for 2*IF-M*, and 25–40% of k_{t^*} for 2*IF-SF*, compared to a 25–50% contribution found experimentally using spectral inte-

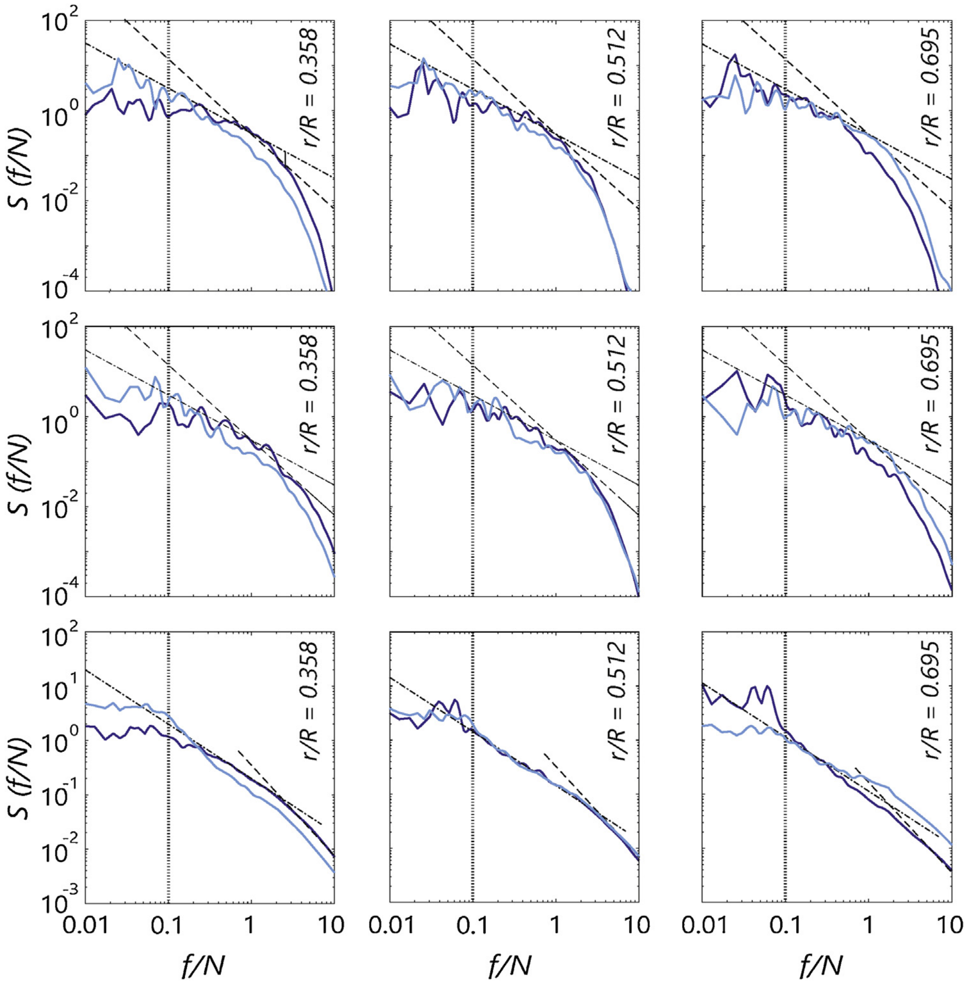

Fig. 8 – Spectral density functions of u'_{ax} (dark blue) and u'_{rad} (light blue) at 3 radial positions, in the plane y = 0. (A) 2*IF-M* LES. (B) 2*IF-SF* LES. (C) Experimental results. Dashed line: $S(f/N) \propto (f/N)^{-5/3}$. Dash-dot line: $S(f/N) \propto (f/N)^{-1}$. Dotted line: cut-off frequency between MI and turbulence. (For interpretation of the references to color in this figure legend, the reader is referred to the web version of this article.)

gration. The difference between auto-correlation fitting and spectral integration arising due to the inclusion of limited frequencies in the former, and all low-frequency components in the latter. Next, we compare the profiles of velocity and kinetic energy in the inter-compartment region. Because of the more straightforward comparison with experimental data, the spectral integration method is used to determine the MI contribution in the kinetic energy data presented in Fig. 9.

Aside from an offset at the baffle position, which is attributed to the 2D baffle geometry, U_{rad} is well captured (Fig. 9). The change from converging to diverging flow in U_{ax} is excellently assessed by all but the crudest mesh. Overall good agreement in k_t is observed (despite the poorer performance in the impeller discharge stream), with 2*IF-M* over-estimative near the shaft, whereas 2*IF-SF* is so near the baffle. Both simulations reasonably capture $k_{MI,SI}$ near the shaft, but only with mesh 2*IF-SF* the peak at $r/R = 0.694$ is properly captured. Even though the frequency distribution does not completely agree with experiments, the overall $k_{MI,SI}$ and $k_{t,SI}$ are well captured by 2*IF-SF*, in line with the good assessment of θ_{95}. The slight under-estimation of θ_{95} by the crude and medium mesh may be by virtue of their higher k_t near the shaft: axial transport of tracer is strongest at this location, as was shown in the mixing snapshots for the *SM-RANS* simulations.

5. Concluding remarks

In this work, we report sliding mesh (SM) and large eddy simulations (LES) of a stirred tank with 2 Rushton impellers at large mutual clearance. Earlier studies reported (1) experimental evidence for macro-instabilities (MIs) in a 2-Rushton stirred tank, (2) an over-estimation of mixing time θ_{95} with the multiple reference frame (MRF) simulation model, increasing with mesh density, (3) a milder over-estimation of θ_{95} with SM, and slight under-prediction of θ_{95} with LES.

Compartment formation around the impellers leads to a parallel radial flow in the inter-compartment plane, causing poor mass exchange between the compartments, thereby forming a rate limiting step in mixing. Our hypothesis was that RANS simulations over-predict θ_{95}, as Reynolds averaging leads to a near-shear free flow in the inter-compartment plane, which fails to properly capture the generation of turbulence by the colliding flow. This in turn leads to a local under-predicting turbulent viscosity μ_t. Both SM simulations and MRF simulations (Part I) indeed under-predicted k_t in the inter-compartment region, compared to LDA measurements, which supports this hypothesis. Additionally, macro-instabilities (MIs) were observed to contain around 30% of the fluctuating kinetic energy k_{t^*} in the inter-compartment plane; these MIs can strongly impact mixing. The SM simulations did pre-

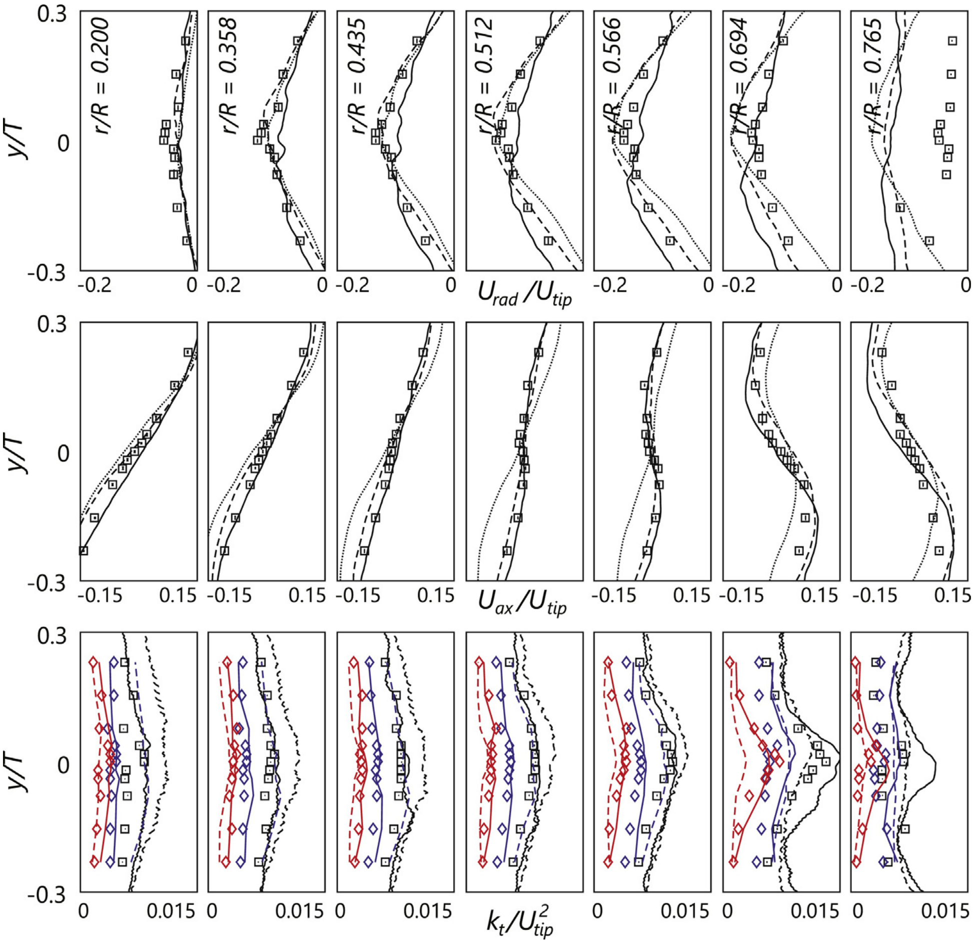

Fig. 9 – Axial profiles (baffle plane) of (A): U_{rad}, (B): U_{ax}, (C): k_t, comparing LDA results (symbols) with LES-CFD data (lines). In (C), the black rectangles represent the total kinetic energy k_{t^*}, the blue diamonds the turbulent kinetic energy k_t, and the red diamonds the MI energy k_{MI}. The black lines represent k_{t^*}, the blue lines k_t, the red lines k_{MI}. Lines: CFD results at different mesh densities (dotted: 2IF – C, dashed: 2IF – M, solid: 2IF – SF. (For interpretation of the references to color in this figure legend, the reader is referred to the web version of this article.)

dict the presence of such MIs, albeit slightly under-estimating their kinetic energy, whereas the frozen-flowfield MRF simulations by construction do not predict them. Overall, the under-predicted k_t causes θ_{95} to be over-predicted by both *SM-RANS* and *MRF-RANS*, but the inclusion of MIs means the over-prediction by *SM-RANS* is less severe; approximately 20% by SM-RKE with realizable $k-\epsilon$ (which outperformed *SM-RSM*), while an over-estimation of near 60% was observed with MRF at same mesh. In this work, we have used structured hexahedral meshes. The results may be different at unstructured meshes of similar resolution, but the over-predictions are expected to hold once mesh independence is achieved.

Turbulent Schmidt number (Sc_t) tuning was suggested to improve agreement in θ_{95} on some occasions (Montante et al., 2005; Gunyol and Mudde, 2009). The current results suggests such tuning is not based on physical considerations, but as a patchwork solution to repair an inadequate estimation of k_t (hence μ_t and the effect of MIs on multi-impeller mixing behavior. While such a patch be an adequate solution if approximate mixing dynamics suffice, the limitations of multi-impeller RANS simulations must be kept in mind, and the RANS models studied in the current work (realizable $k-\epsilon$ and *RSM*) seem inadequate for quantitative mixing assessment in multi-impeller systems.

The mixing time was under-estimated approx. 13% with LES at crude meshes (below 2 million grid cells), in accordance with Jahoda et al. (2007). With a mesh of approx. 10 million cells, θ_{95} was in excellent agreement with experiments. The MI frequencies in the inter-compartment region as predicted in LES simulations are not as sharply distinguishable as in the LDA data, and differences in the dominant frequencies are observed. At the crude- and medium mesh, k_{MI} was still under-predicted in general, but higher near the shaft, higher values were observed than experimentally. The region near the shaft is where most mass exchange between the compartments is predicted to take place, which may explain the lower θ_{95} with a cruder mesh. Despite the difference in frequencies, k_{MI} is in good agreement between the fine-mesh LES and experiments, as is k_t.

The applied LES approach did over-predict k_t and under-predict ϵ in the impeller discharge stream. This is attributed to the employed dynamic Smagorinsky model, which predicts low values of constant C_S. While taking C_S constant and fine-tuning it may increase agreement (Delafosse et al., 2014), a more universal approach is desired. As such, there is room for further exploration of LES and other transient simulation approaches ((ID)DES, hybrid LES-RANS, etc.) in stirred tank applications. Strictly speaking, the finest current LES study was under-resolved, especially in the impeller region. Higher resolution studies may be desirable for further fundamental studies, but already the current fine mesh is considered too demanding for routine mixing studies. Despite the in predicting ϵ, LES performed well in terms of mixing assessment, even on the crudest meshes which far from resolve all energy carrying turbulence scales. As both SM and LES mispredict θ_{95} to a similar degree at the crude meshes, and both have similar computational demands, both are currently considered to be reasonably options for mixing assessment provided their degree of error is kept in account; both are clearly preferred above MRF. However, if computational facilities allow for finer meshes, LES is the preferred choice.

Acknowledgements

We wish to thank our colleagues at ECUST, Shanghai and DSM Sinochem pharmaceuticals for our ongoing collaboration. We are grateful to Prof. H. van den Akker, Dr. S. Kenjeres, Dr. L. Portela and Prof. H.J. Noorman for their advice and insights. CH acknowledges all students following M.Sc. course CH3421, who contributed to the simulation results as part of their course reports. Evert Wagner, Jos Thieme, Christiaan Schinkel, Stefan ten Hagen, Youp van Goozen and Ruud van Tol are gratefully acknowledged for their technical assistance. This work has been conducted within a multi-party research project, between DSM-Sinochem Pharmaceuticals, TU Delft, East China University of Science and Technology and Guojia, subsidized by NWO and MoST (NWO-MoST Joint program 2013DFG32630). All sponsors are gratefully acknowledged.

Appendix A. Supplementary data

Supplementary data associated with this article can be found, in the online version, at https://doi.org/10.1016/j.cherd.2018.06.007.

References

Bakker, R., 1996. Laser-Doppler Measurements in a Baffled Stirred Tank Reactor With a Disc Turbine (Ph.D. thesis). Delft University of Technology.

Chara, Z., Kysela, B., Konfrst, J., Fort, I., 2016. Study of fluid flow in baffled vessels stirred by a Rushton standard impeller. Appl. Math. Comput. 272, 614–628, http://dx.doi.org/10.1016/j.amc.2015.06.044.

Coroneo, M., Montante, G., Paglianti, A., Magelli, F., 2011. CFD prediction of fluid flow and mixing in stirred tanks: numerical issues about the RANS simulations. Comput. Chem. Eng. 35 (10), 1959–1968, http://dx.doi.org/10.1016/j.compchemeng.2010.12.007.

Delafosse, A., Liné, A., Morchain, J., Guiraud, P., 2008. LES and URANS simulations of hydrodynamics in mixing tank: comparison to PIV experiments. Chem. Eng. Res. Des. 86 (12), 1322–1330, http://dx.doi.org/10.1016/j.cherd.2008.07.008.

Delafosse, A., Morchain, J., Guiraud, P., Liné, A., 2009. Trailing vortices generated by a Rushton turbine: assessment of URANS and large Eddy simulations. Chem. Eng. Res. Des. 87 (4), 401–411, http://dx.doi.org/10.1016/j.cherd.2008.12.018.

Delafosse, A., Collignon, M.-L., Calvo, S., Delvigne, F., Crine, M., Thonart, P., Toye, D., 2014. CFD-based compartment model for description of mixing in bioreactors. Chem. Eng. Sci. 106, 76–85 http://www.sciencedirect.com/science/article/pii/S0009250913007690.

Derksen, J., Van den Akker, H.E.A., 1999. Large eddy simulations on the flow driven by a Rushton turbine. AIChE J. 45 (2), 209–221, http://dx.doi.org/10.1002/aic.690450202.

Derksen, J., Doelman, M., Van den Akker, H., 1999. Three-dimensional LDA measurements in the impeller region of a turbulently stirred tank. Exp. Fluids 27 (6), 522–532, http://dx.doi.org/10.1007/s003480050376.

Ducci, A., Yianneskis, M., 2005. Direct determination of energy dissipation in stirred vessels with two-point LDA. AIChE J. 51 (8), 2133–2149, http://dx.doi.org/10.1002/aic.10468.

Eggels, J.G.M., 1996. Direct and large-eddy simulation of turbulent fluid flow using the lattice-Boltzmann scheme. Int. J. Heat Fluid Flow 17 (3), 307–323, http://dx.doi.org/10.1016/0142-727X(96)00044-6.

Escudié, R., Bouyer, D., Liné, A., 2004. Characterization of trailing vortices generated by a Rushton turbine. AIChE J. 50 (1), 75–86, http://dx.doi.org/10.1002/aic.10007.

Germano, M., Piomelli, U., Moin, P., Cabot, W.H., 1990. A dynamic subgrid-scale eddy viscosity model. In: Studying Turbulence Using Numerical Simulation Databases. 3: Proceedings of the 1990 Summer Program, Stanford Univ, pp. 5–17 (SEE N92-30648 21-34). http://adsabs.harvard.edu/abs/1990stun.proc..5G.

Gillissen, J.J.J., Van den Akker, H.E.A., 2012. Direct numerical simulation of the turbulent flow in a baffled tank driven by a Rushton turbine. AIChE J. 58 (12), 3878–3890, http://dx.doi.org/10.1002/aic.13762.

Gimbun, J., Rielly, C.D., Nagy, Z.K., Derksen, J.J., 2012. Detached eddy simulation on the turbulent flow in a stirred tank. AIChE J. 58 (10), 3224–3241, http://dx.doi.org/10.1002/aic.12807.

Gunyol, O., Mudde, R.F., 2009. Computational study of hydrodynamics of a standard stirred tank reactor and a large-scale multi-impeller fermenter. Int. J. Multisc. Comput. Eng. 7 (6), 559–576.

Hartmann, H., Derksen, J., Montavon, C., Pearson, J., Hamill, I., van den Akker, H., 2004. Assessment of large eddy and RANS stirred tank simulations by means of LDA. Chem. Eng. Sci. 59 (12), 2419–2432, http://dx.doi.org/10.1016/j.ces.2004.01.065.

Hartmann, H., Derksen, J.J., van den Akker, H.E.A., 2006. Mixing times in a turbulent stirred tank by means of LES. AIChE J. 52 (11), 3696–3706, http://dx.doi.org/10.1002/aic.10997.

Jahoda, M., Moštěk, M., Kukuková, A., Machon, V., 2007. CFD modelling of liquid homogenization in stirred tanks with one and two impellers using large Eddy simulation. Chem. Eng. Res. Des. 85 (5), 616–625, http://dx.doi.org/10.1205/cherd06183.

Kim, S.-E., et al., 2004. Large eddy simulation using unstructured meshes and dynamic subgrid-scale turbulence models. AIAA Paper, 34th Fluid Dynamics Conference and Exhibit 2548.

Lane, G., 2015. Predicting the energy dissipation rate in a mechanically stirred tank. In: Eleventh International Conference on CFD in the Minerals and Process Industries. CSIRO Australia, Melbourne, Australia http://www.cfd.com.au/cfd_conf15/PDFs/129LAN.pdf.

Lilly, D.K., 1992. A proposed modification of the Germano subgrid? Scale closure method. Phys. Fluids A: Fluid Dyn. 4 (3), 633–635, http://dx.doi.org/10.1063/1.858280.

Micheletti, M., Baldi, S., Yeoh, S., Ducci, A., Papadakis, G., Lee, K., Yianneskis, M., 2004. On spatial and temporal variations and estimates of energy dissipation in stirred reactors. Chem. Eng. Res. Des. 82 (9), 1188–1198, http://dx.doi.org/10.1205/cerd.82.9.1188.44172.

Montante, G., Moštěk, M., Jahoda, M., Magelli, F., 2005. CFD simulations and experimental validation of homogenisation curves and mixing time in stirred Newtonian and pseudoplastic liquids. Chem. Eng. Sci. 60 (8-9), 2427–2437, http://dx.doi.org/10.1016/j.ces.2004.11.020.

Murthy, B., Joshi, J., 2008. Assessment of standard, RSM and LES turbulence models in a baffled stirred vessel agitated by various impeller designs. Chem. Eng. Sci. 63 (22), 5468–5495, http://dx.doi.org/10.1016/j.ces.2008.06.019.

Paglianti, A., Liu, Z., Montante, G., Magelli, F., 2008. Effect of macroinstabilities in single- and multiple-impeller stirred tanks. Ind. Eng. Chem. Res. 47 (14), 4944–4952, http://dx.doi.org/10.1021/ie800253u.

Ranade, V.V., Joshi, J.B., 1990. Flow generated by a disc turbine. II. Mathematical modelling and comparison with experimental data. Chem. Eng. Res. Des. 68 (1), 34–50 http://cat.inist.fr/?aModele=afficheN&cpsidt=6817059.

Revstedt, J., Fuchs, L., Trägårdh, C., 1998. Large Eddy simulations of the turbulent flow in a stirred reactor. Chem. Eng. Sci. 53

(24), 4041–4053, http://dx.doi.org/10.1016/S0009-2509(98)00203-6.

Singh, H., Fletcher, D.F., Nijdam, J.J., 2011. An assessment of different turbulence models for predicting flow in a baffled tank stirred with a Rushton turbine. Chem. Eng. Sci. 66 (23), 5976–5988, http://dx.doi.org/10.1016/j.ces.2011.08.018.

Soos, M., Kaufmann, R., Winteler, R., Kroupa, M., Lüthi, B., 2013. Determination of maximum turbulent energy dissipation rate generated by a Rushton impeller through large eddy simulation. AIChE J. 59 (10), 3642–3658, http://dx.doi.org/10.1002/aic.14206.

Wu, H., Patterson, G., 1989. Laser-Doppler measurements of turbulent-flow parameters in a stirred mixer. Chem. Eng. Sci. 44 (10), 2207–2221, http://dx.doi.org/10.1016/0009-2509(89)85155-3.

Yeoh, S., Papadakis, G., Yianneskis, M., 2004. Numerical simulation of turbulent flow characteristics in a stirred vessel using the LES and RANS approaches with the sliding/deforming mesh methodology. Chem. Eng. Res. Des. 82 (7), 834–848, http://dx.doi.org/10.1205/0263876041596751.

Yeoh, S., Papadakis, G., Yianneskis, M., 2005. Determination of mixing time and degree of homogeneity in stirred vessels with large eddy simulation. Chem. Eng. Sci. 60 (8-9), 2293–2302, http://dx.doi.org/10.1016/j.ces.2004.10.048.

Zhang, Y., Yang, C., Mao, Z., 2006. Large Eddy simulation of liquid flow in a stirred tank with improved inner-outer iterative algorithm. Chin. J. Chem. Eng. 14 (3), 321–329, http://dx.doi.org/10.1016/S1004-9541(06)60078-5.